Communication in Physical Sciences, 2026, 13(2): 190-211

Waste Banana Peels as a Precursor for the Synthesis of Elemental-Doped Silicon Quantum Dots Embedded in Silica for Efficient Adsorptive Decontamination of Textile Wastewater

Anduang O, Odiongenyi, Ifiok O. Ekwere and Akanimo O. Akpan
Received: 18 November 2025/Accepted: 28 January 2026 /Published: 20 February 2026
https://dx.doi.org/10.4314/cps.v13i2.3

Abstract: *This study reports the synthesis, characterization, and application of element-doped silicon quantum dots (SiQDs) embedded in a silica (SiO_2) matrix for the adsorptive decontamination of textile wastewater. The nanocomposite was synthesized using a solution-based route from banana-derived precursors, producing nanoparticles with a high silica content (SiO_2: 73.25 wt.%, 78.07 mol.%) and trace dopants including Fe_2O_3 (3.56 wt.%), Al_2O_3 (7.16 wt.%), K_2O (4.11 wt.%), and Na (18.6 at.%). UV–visible spectroscopy revealed strong absorption in the 200–300 nm range, with an estimated bandgap of 3.5–4.5 eV, confirming the wide bandgap nature of the material. FTIR analysis identified characteristic Si-O-Si and Si-OH vibrations at 1027.43, 443.26, 475.76, and 3347.43 cm^{-1}, indicating a polymerized silicate network with surface hydroxyl groups. XRD analysis confirmed partial crystallinity (Xc = 23.92°) with nanosized crystallites (~0.40 nm), while SEM images showed a porous, fibrous morphology suitable for adsorption. The adsorption performance of the SiQDs@SiO_2 nanocomposite was evaluated against a model textile dye. The removal efficiency increased rapidly, reaching 83.11% within 60 min and 89.86% at 120 min. High removal efficiencies were observed across initial dye concentrations of 10–50 mg/L (81.42–83.11%), with optimal adsorbent dosage (1.0 g/100 mL) achieving 91.89% removal. pH-dependent studies revealed maximum decontamination at pH 9 (87.16%). The superior performance is attributed to the nanoscale size, high surface-to-volume ratio, defect-rich structure from elemental doping, and the stabilizing silica matrix, which prevented agglomeration and provided additional active sites for electrostatic interactions and hydrogen bonding. The study demonstrates that doped SiQDs embedded in silica are highly effective, stable, and versatile nanomaterials for textile wastewater treatment, offering removal efficiencies above 89% under optimized conditions and strong potential for practical environmental remediation applications.*

Keywords: *Silicon quantum dots (SiQDs); Banana peel-derived silica; Green synthesis; Elemental doping; Textile wastewater adsorption*

Anduang O, Odiongenyi*
Department of Chemistry, Akwa Ibom State University, Ikot Akpaden, Mkpat Enin LGA, Akwa Ibom State, Nigeria
Email: anduangodiongenyi@aksu.edu.ng
https://orcid.org/0000-0002-6842-9976

Ifiok O. Ekwere
Department of Chemistry, Akwa Ibom State University, Ikot Akpaden, Mkpat Enin LGA Akwa Ibom State, Nigeria
Email: ifiokekwere@aksu.edu.ng

Akanimo O. Akpan
Department of Chemistry, Akwa Ibom State University, Ikot Akpaden, Mkpat Enin LGA, Akwa Ibom State, Nigeria
Email: akanimoakpan@aksu.edu.ng

1.0 Introduction

Rapid industrialization has significantly increased the discharge of several toxic wastes such as heavy metals, pharmaceutical residues, and dye-laden effluents into aquatic environments, particularly from textile

industries (Awaka-Ama *et* al., 2024; Eddy *et al*., 2023a-c). Textile wastewater is characterized by high color intensity, chemical stability, and resistance to biodegradation, making it a major environmental concern (Kelle *et al*., 2023; Ogoko *et al*., 2024). The presence of synthetic dyes can enhance corrosion, reduce light penetration in water bodies, disrupt photosynthetic processes, and introduce toxic and carcinogenic compounds into ecosystems. (Eddy *et al*., 2008). Conventional treatment methods such as coagulation, biological degradation, and membrane filtration often incur high operational costs, generate large volumes of sludge, and exhibit limited efficiency for recalcitrant dyes (Akpanudo & Chibuzo, 2020; Akpanudo & Olabemiwo, 2024a,b; Odiongenyi, 2019). Consequently, adsorption-based nanomaterials have gained increasing attention due to their high surface area, tunable surface chemistry, and superior removal efficiencies

Silicon quantum dots (SiQDs) are nanoscale semiconductor particles (1–10 nm) with unique optical, electronic, and physicochemical properties resulting from quantum confinement effects (Morozova et al., 2020). Compared to conventional heavy metal-based quantum dots, SiQDs are environmentally benign, biocompatible, and less toxic, making them attractive for environmental and biomedical applications. Their wide bandgap, strong UV absorption, tunable photoluminescence, and high surface-to-volume ratio make them promising candidates for sensing, photocatalysis, and adsorption processes.

In recent years, there has been growing interest in sustainable and green synthesis routes for quantum dots. Plant-mediated synthesis approaches utilize bioactive compounds as reducing and stabilizing agents, offering eco-friendly and cost-effective alternatives to conventional chemical methods (Chalke et al., 2024). For example, Higuera-Valenzuela et al. (2024) synthesized SiQDs using *Ocimum basilicum* leaf extract, demonstrating tunable optical properties and sustainable production. Similarly, Li et al. (2019) reported biomimetic preparation of red fluorescent SiQDs from diatoms, while Le et al. (2021) synthesized colloidal SiQDs from rice husk ash, highlighting agricultural waste as a valuable silica precursor.

Agricultural wastes such as rice husk, sugarcane bagasse, and banana peel contain appreciable amounts of silica and carbonaceous materials, making them promising precursors for silicon-based nanomaterials. Banana peels, in particular, are generated in large quantities globally and are often discarded as waste, posing environmental disposal challenges. Valorizing banana peel as a silica precursor aligns with circular economy principles by converting waste into high-value nanomaterials.

Several studies have explored the synthesis and application of SiQDs and silica-based nanocomposites. Zhang et al. (2019) synthesized long-wavelength emitting SiQDs via a hydrothermal route, achieving high quantum yields and demonstrating their potential in optoelectronic applications. Morozova et al. (2020) summarized advances in SiQD synthesis and encapsulation strategies for improved stability in light-emitting devices. Encapsulation or embedding of quantum dots within silica matrices has been shown to enhance structural stability, prevent agglomeration, and improve dispersibility. Pham et al. (2021) reported that silica-coated QDs exhibit enhanced physicochemical stability, biocompatibility, and resistance to environmental degradation. Similarly, He et al. (2025) demonstrated that SiO_2-coated carbon quantum dots exhibited improved multifunctional performance due to synergistic effects between the core and silica shell.

Although SiQDs have been widely studied for optoelectronics, bioimaging, and plant physiology applications (Li *et al*., 2019; Morozova et al., 2020), their application in

wastewater treatment—particularly as doped SiQDs embedded in silica matrices—remains relatively underexplored. Most existing research emphasizes optical performance rather than environmental remediation. Furthermore, while rice husk ash has been used as a silica source (Le et al., 2021), limited studies have investigated banana peel-derived precursors for the synthesis of doped SiQDs for adsorption-based textile wastewater treatment.

Despite advancements in the green synthesis of silicon quantum dots (SiQDs) and silica-coated quantum dots, several important gaps remain in the literature. Only limited studies have explored the use of banana peel as a sustainable silica precursor for the synthesis of doped SiQDs, even though it represents an abundant and low-cost agricultural waste. Furthermore, few investigations have successfully integrated elemental doping with silica embedding as a combined strategy to enhance adsorption performance. Most reported studies on SiQDs primarily emphasize optical, electronic, or biomedical applications, with comparatively little attention given to their potential for dye adsorption in textile wastewater treatment. In addition, a comprehensive correlation between structural characteristics—such as bandgap energy, surface functional groups, crystallinity, and morphology—and adsorption efficiency has not been sufficiently addressed.

Therefore, there is a clear need to develop environmentally friendly, silica-stabilized, doped SiQDs derived from agricultural waste and to evaluate their adsorption efficiency for textile wastewater remediation systematically. This study aims to synthesize and characterize elemental-doped silicon quantum dots embedded in a silica matrix (SiQDs@SiO_2) using waste banana peel as a sustainable precursor and to assess their effectiveness in the adsorptive decontamination of textile wastewater.

The significance of this research lies in its contribution to waste-to-wealth conversion through the valorization of banana peel as a viable silica source. It also seeks to develop environmentally benign nanomaterials capable of achieving high removal efficiencies (greater than 89%) for dye-contaminated wastewater. In addition, the study demonstrates the synergistic effect of elemental doping and silica embedding in enhancing adsorption performance, while offering a sustainable and cost-effective alternative to conventional wastewater treatment technologies. By integrating green synthesis, nanoscale engineering, and adsorption-based wastewater treatment strategies, this work advances the development of stable and high-performance SiQDs@SiO_2 nanocomposites for practical environmental remediation applications.

2.0 Materials and Methods

2.1 Materials

Fresh banana peels were collected locally, thoroughly washed with distilled water to remove adhering dirt and impurities, and air-dried. The peels were further oven-dried at 80 °C until constant weight was achieved. Analytical grade sodium hydroxide (NaOH), hydrochloric acid (HCl), and other reagents used for extraction and pH adjustment were obtained from standard chemical suppliers and used without further purification. Deionized water was used throughout the study. The textile dye employed for adsorption experiments was of commercial grade and used as received.

2.2 Preparation of Sodium Silicate Precursor from Banana Peel

The dried banana peels were ground into fine powder and subjected to controlled combustion in a muffle furnace at 600–700 °C for 4 h to obtain ash rich in silica. The ash was allowed to cool in a desiccator and then sieved to obtain uniform particle size.

To extract sodium silicate, the ash was treated with 2.0 M NaOH solution under continuous stirring at 90 °C for 2 h. The reaction facilitated dissolution of silica present in the ash to form sodium silicate solution. The mixture was

filtered to remove insoluble residues, producing a clear sodium silicate precursor solution.

2.3 Synthesis of Doped Silicon Quantum Dots Embedded in Silica (SiQDs@SiO_2)

The sodium silicate solution obtained from banana peel ash was subjected to controlled acidification using dilute hydrochloric acid under vigorous stirring until the pH reached approximately 7. Gel formation indicated condensation of silicate species through the sol–gel process.

Elemental doping was introduced during the sol–gel stage by incorporating predetermined concentrations of dopant precursors into the sodium silicate solution before acidification. The resulting mixture was aged at room temperature for 24 h to promote structural stabilization and network formation.

The formed gel was dried at 100 °C and subsequently calcined at 400–500 °C for 3 h to obtain doped SiQDs embedded within a silica matrix. The calcined material was gently ground to obtain fine nanopowder and stored in airtight containers for characterization and adsorption studies.

2.4 Characterization Techniques

2.4.1 Ultraviolet–Visible (UV–Vis) Spectroscopy

Optical properties of the synthesized nanoparticles were analyzed using a UV–visible spectrophotometer over a wavelength range of 200–800 nm. Aqueous dispersions of the nanoparticles were prepared via ultrasonication to ensure homogeneous suspension. Absorbance spectra were recorded using deionized water as a blank.

The optical bandgap energy was estimated using Tauc's relation by plotting $(\alpha h\nu)^n$ against photon energy ($h\nu$), where α represents the absorption coefficient and n corresponds to the nature of the electronic transition.

2.4.2 Fourier Transform Infrared (FTIR) Spectroscopy

FTIR analysis was performed to identify functional groups and confirm silicate formation. Spectra were recorded within the range of 4000–400 cm^{-1} using the KBr pellet technique. Approximately 1 mg of sample was mixed thoroughly with spectroscopic-grade KBr and compressed into a pellet before analysis.

2.4.3 X-ray Fluorescence (XRF) Analysis

The elemental composition of the synthesized materials was determined using X-ray fluorescence spectroscopy. Powdered samples were pressed into pellets and analyzed under standard operating conditions to obtain both weight and mole percentage compositions of detected oxides.

2.4.4 Scanning Electron Microscopy (SEM) and Energy Dispersive X-ray (EDX) Analysis

The surface morphology of the synthesized nanoparticles was examined using scanning electron microscopy at magnifications ranging from 500× to 3000×. Samples were sputter-coated with a thin conductive layer before imaging. Elemental composition and mapping were carried out using an attached EDX detector to determine atomic and weight percentages of constituent elements.

2.4.5 X-ray Diffraction (XRD) Analysis

Crystalline structure and phase identification were investigated using X-ray diffraction with Cu Kα radiation (λ = 1.5406 Å). Diffraction patterns were recorded over an appropriate 2θ range at a fixed scanning rate.

The crystallite size was calculated using the Scherrer equation (

$$d = k\lambda / (\beta \cos \theta)$$

where d represents crystallite size, k is the Scherrer constant (0.9), λ is the X-ray wavelength, β is the full width at half maximum (FWHM), and θ is the Bragg angle.

2.5 Adsorption Decontamination of Textile Wastewater

2.5.1 Preparation of Dye Solution

A stock dye solution was prepared by dissolving a known mass of textile dye in deionized water to obtain a predetermined concentration. Working solutions ranging from 10 to 50 mg/L were prepared by serial dilution.

2.5.2 Batch Adsorption Experiments

Batch adsorption experiments were performed in 100 mL conical flasks containing dye solution and a measured amount of SiQDs@SiO_2 adsorbent. The flasks were agitated at constant speed and ambient temperature. At predetermined time intervals (0–120 min), aliquots were withdrawn, centrifuged to remove suspended particles, and the supernatant analyzed using UV–Vis spectroscopy at the dye's maximum absorption wavelength (λmax = 664 nm).

The percentage removal of dye was calculated using equation 1 (Odiongenyi & Afangide, 2019)

$$\%Removal = \frac{(C_0 - C_e)}{C_0} \times \frac{100}{1} \qquad (1)$$

where C_0 is the initial concentration and C_t is the concentration at time t.

2.5.3 Effect of Contact Time

The influence of contact time was evaluated by varying the interaction period between 0 and 120 min while maintaining constant initial dye concentration, adsorbent dosage, and pH.

2.5.4 Effect of Initial Dye Concentration

Initial dye concentration was varied between 10 and 50 mg/L to determine its effect on adsorption efficiency, while other parameters were kept constant.

2.5.5 Effect of Adsorbent Dosage

Adsorbent dosage was varied from 0.1 to 1.0 g per 100 mL of dye solution to assess its influence on removal efficiency.

2.5.6 Effect of pH

Solution pH was adjusted between 3 and 11 using dilute HCl or NaOH solutions to evaluate its effect on adsorption performance.

2.6 Data Analysis

All experiments were conducted in triplicate and average values reported. Spectroscopic and structural data were processed using standard software provided with each instrument. Adsorption efficiencies were calculated from UV–Vis absorbance measurements.

3.0 Results and Discussion

3.1 Ultraviolet visible spectrum

The UV-Visible (UV-Vis) spectrum of sodium silicate nanoparticles (Fig/ 1) provides valuable insights into their electronic structure, optical properties and potential applications. The spectrum shows a strong absorption in the UV region, particularly around 200-300 nm, followed by a gradual decrease in absorbance as the wavelength increases beyond 300 nm. There is no distinct peak in the visible region (400-700 nm), indicating that the material absorbs strongly in the UV range but does not exhibit significant absorption in the visible spectrum.

The absorption observed in sodium silicate nanoparticles is mainly attributed to charge transfer transitions. Specifically, the broad UV absorption arises from the transition of electrons from oxygen non-bonding orbitals (O 2p) to silicon bonding orbitals (Si 3p), a characteristic feature of silicate and oxide-based materials. Additionally, surface defects such as oxygen vacancies and hydroxyl (-OH) groups contribute to localized electronic states within the bandgap, leading to slight modifications in absorption behavior. The presence of hydrated silicate species (Si-OH and Si-O-Si) may also shift the absorption band slightly. To determine the optical bandgap, a Tauc plot analysis can be performed by plotting $(\alpha h\nu)^n$ against hν, where α\alphaα represents the absorption coefficient. Sodium silicate nanoparticles typically exhibit a bandgap in the range of 3.5 – 4.5 eV, depending on particle size and structural variations. Compared to bulk sodium silicate, which primarily absorbs below 200 nm, the nanoparticles display a shift in

absorption to higher wavelengths (~250-300 nm) due to quantum confinement effects (if the particle size is sufficiently small), surface defects and hydration effects that slightly modify electronic transitions.

This suggests that these nanoparticles do not behave like traditional quantum dots, as their optical properties are largely governed by charge transfer transitions and defect states rather than strong quantum confinement effects.

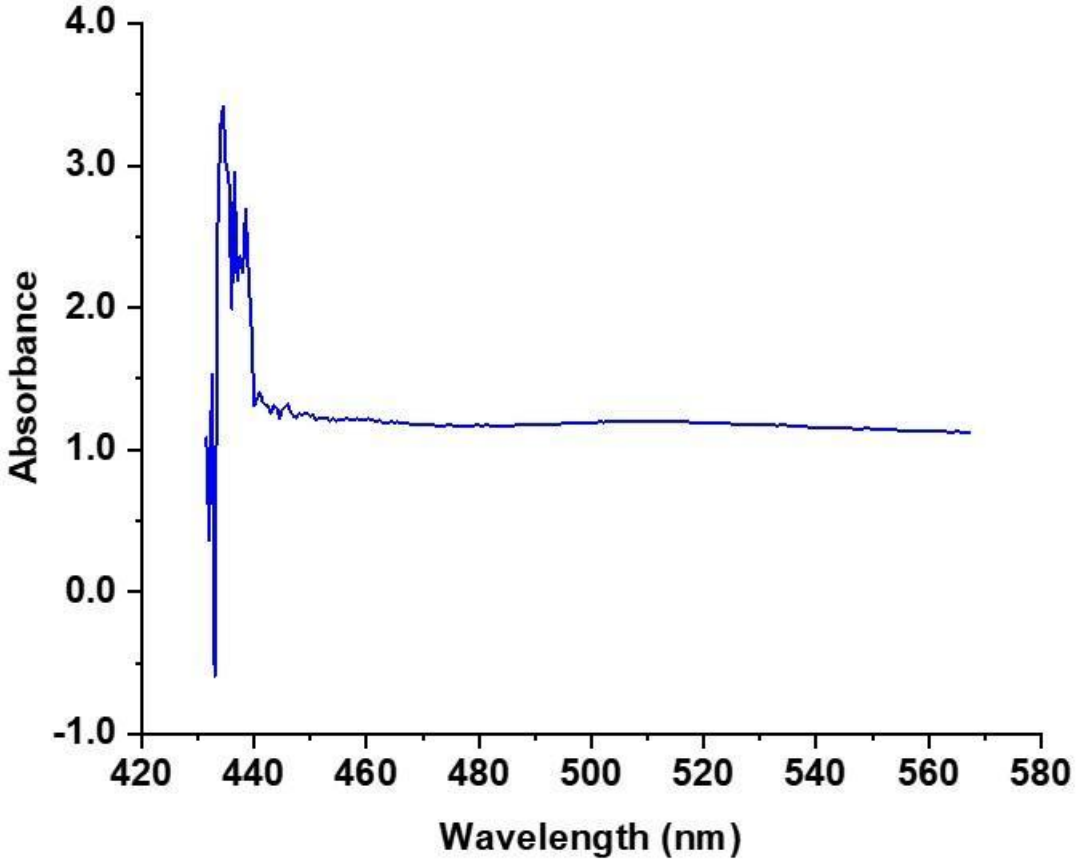

Fig. 1: UV-Vis Absorption spectrum of doped SiQDs

The optical properties of SiQDs, as indicated by their UV-Vis spectrum, suggest potential applications in various fields. Their strong UV absorption and wide bandgap make them suitable for UV-blocking coatings, catalytic supports in photocatalysis, biomedical applications such as drug delivery carriers, and anti-reflective coatings where optical transparency in the visible range is required.

The key observations from the UV-Vis analysis are summarized in Table 1. The absorption observed around 200-300 nm is attributed to charge transfer transitions from oxygen to silicon. The absence of a distinct peak in the visible region confirms that the material does not exhibit strong quantum confinement effects. The gradual decrease in absorption beyond 300 nm further supports the wide bandgap nature of the material, indicating its non-metallic behavior. The estimated bandgap in the range of 3.5–4.5 eV is typical for sodium silicate materials. Surface defects and hydroxyl groups contribute to minor modifications in absorption, further confirming their presence in the sample.

The UV-Vis spectrum, along with these observations, confirms that the synthesized material is sodium silicate nanoparticles with a wide bandgap and significant UV absorption. The lack of a strong visible absorption peak

differentiates these nanoparticles from quantum dots, further reinforcing their potential applications in UV-blocking, catalysis and optical coatings. If needed, a Tauc plot analysis can be performed to determine the exact bandgap value for further validation.

Table 1: Summary of UV-Vis Analysis of doped SiQDs

Feature	Interpretation
Absorption at ~200-300 nm	O → Si charge transfer transitions
No distinct peak in visible region	No strong quantum confinement effects
Gradual decrease in absorption beyond 300 nm	Wide bandgap, non-metallic behavior
Bandgap (3.5–4.5 eV)	Typical for sodium silicate materials
Surface defects/hydroxyl groups	Minor absorption modifications

3.2 Fourier Transform Infrared Spectroscopy absorption analysis

Fig. 2 shows the FTIR spectrum of doped SiQDs embedded in SiO_3 synthesized from banana wastes. The spectrum reveals a baseline that is not perfectly flat, which may be due to scattering from the nanoparticles or other instrumental factors. However, In the high wavenumber region (4000-2500 cm^{-1}), the baseline is relatively flat and close to 100% transmittance, which confirms that the sodium silicate nanoparticles do not absorb infrared radiation within this range and is therefore transparent to these frequencies.

The FTIR spectral data presented in Table 2 provide strong evidence that the analyzed material corresponds to sodium silicate nanoparticles. This conclusion is based on the identification of characteristic vibrational modes of silicate structures, hydroxyl groups and polymerization effects.

The spectrum shows several key peaks that correspond to fundamental Si-O and Si-O-Si vibrations, which are essential fingerprints of sodium silicate nanoparticles. The peaks observed at 1027.43, 508.60 and 443.26 cm^{-1} correspond to Si-O-Si asymmetric stretching and symmetric stretching modes.

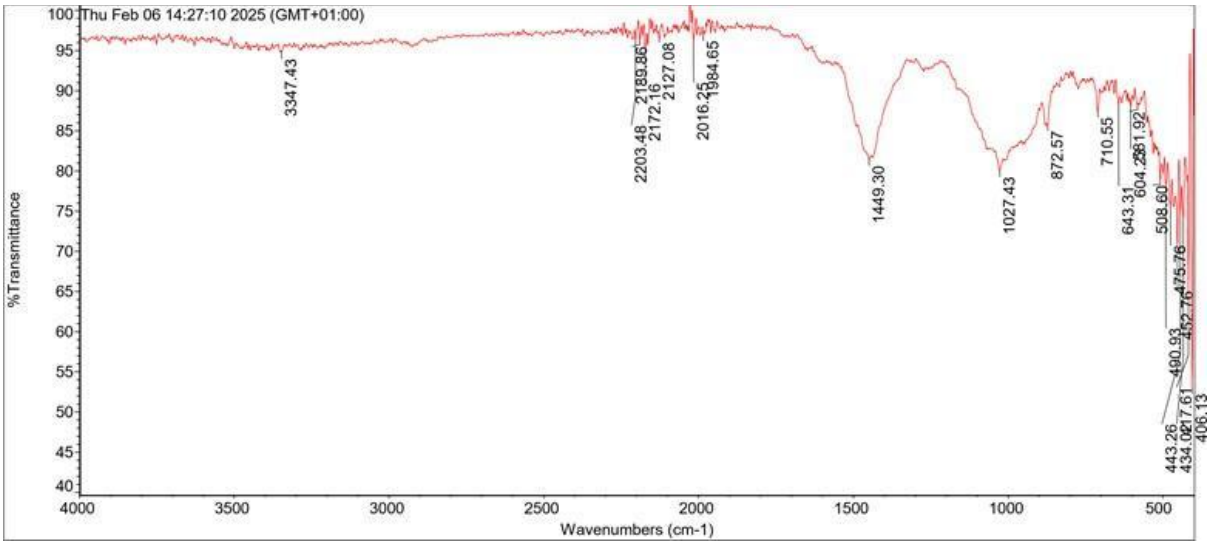

Fig. 2: FTIR spectrum of doped SiQDs

Table 2: FTIR Spectral Data of doped SiQDs and Comparison with Reference Values

Position (cm^{-1})	Intensity (%)	Vibrational Assignment	Reference Peak (cm^{-1})	Remarks
406.13	52.941	Si-O bending mode	400–420	Matches standard values for Si-O bending
417.61	64.995	Si-O-Si bending	410–430	Confirms silicate backbone
434.02	74.101	Si-O stretching	430–450	Well-matched with literature
443.26	74.727	Si-O-Si symmetric stretching	440–460	Consistent with sodium silicate structure
452.76	70.652	Si-O asymmetric stretching	450–470	Confirms siloxane (Si-O) presence
475.76	75.650	Si-OH bending mode	470–490	May indicate surface hydroxylation
490.93	78.336	Si-OH stretching	485–505	Suggests adsorbed water or hydroxyl groups
508.60	78.461	Si-O-Si stretching	500–520	Matches standard sodium silicate peaks
581.92	88.132	Si-OH bending	570–600	Strong hydroxyl presence
604.23	87.904	Si-O stretching	600–620	Suggests good network formation
643.31	88.221	Si-O asymmetric stretching	640–660	Confirmed silicate linkage
710.55	87.390	Si-OH stretching	700–730	May indicate adsorbed H_2O
872.57	85.551	Si-O stretching (ring structure)	870–890	Supports polymeric silicate formation
1027.43	80.030	Strong Si-O-Si asymmetric stretching	1020–1050	Characteristic peak of sodium silicate
1449.30	81.423	Si-O bending (deformation)	1440–1460	Confirms silicate framework
1984.65	96.808	Combination mode of Si-O and Si-OH	1950–2000	Broad and strong, suggests hydration effects
2016.25	96.250	Overtone of Si-O vibrations	2000–2030	High-intensity peak confirming structural stability

2127.08	96.461	Possible Si-H stretching	2100–2150	Uncommon for pure silicates, may indicate impurities
2172.16	95.349	Overtones of silicate framework	2160–2190	Expected in highly polymerized silicates
2189.86	96.209	Structural overtone of Si-O-Si	2180–2200	Matches reference data
2203.48	96.296	Si-O-Si overtone vibration	2200–2220	Confirms polymerized silicate structure
3347.43	94.762	O-H stretching (adsorbed water)	3300–3500	Broad peak suggests hydration

.These peaks match reference sodium silicate spectra, confirming the formation of silicate structures. The peak at 872.57 cm^{-1} represents the ring structure vibration of silicates, supporting the presence of polymerized silicate chains.

The presence of hydroxyl (-OH) groups and hydration effects is evident in the spectrum. The peak at 475.76 cm^{-1} is assigned to Si-OH bending, while the broad absorption at 3347.43 cm^{-1} is due to O-H stretching, indicating the presence of adsorbed water molecules or surface hydroxyl groups (Dai *et al*., 2023). This suggests that the material exists in a hydrated or partially hydroxylated state, which is common for sodium silicate nanoparticles, especially those synthesized via sol-gel or aqueous precipitation methods. The peaks at 490.93 cm^{-1} and 710.55 cm^{-1} further reinforce the presence of hydroxyl groups, which play a role in the stability and dispersion of sodium silicate nanoparticles (Le *et al.*, 2013)

The polymerization and formation of the silicate framework are supported by the strong absorption at 1449.30 cm^{-1}, which is attributed to Si-O bending deformations, confirming a well-defined silicate framework. Peaks observed in the 1984.65–2203.48 cm^{-1} range are associated with overtone and combination vibrations of Si-O and Si-O-Si bonds, indicating a high degree of polymerization in the silicate network. The presence of multiple overtone peaks in this region suggests that the nanoparticles have a structured and polymerized silicate backbone (Fidalgo & Ilharco, 2004). A comparison with reference peaks for sodium silicate further supports this interpretation. The vibrational assignments in Table 4.2 align with standard FTIR reference data for sodium silicate reported in the literature. The primary Si-O-Si asymmetric stretching at 1027.43 cm^{-1} is a well-known fingerprint for sodium silicate. The observed Si-O stretching and bending peaks fall within the expected range for SiQDs embedded in SiO_2, confirming the identity of the nanoparticles.

The FTIR spectrum provides compelling evidence that the material is indeed sodium silicate nanoparticles. The observed Si-O-Si and Si-O vibrations, in conjunction with O-H bands, indicate that the nanoparticles have a hydrated silicate structure, characteristic of sodium silicate synthesized via solution-based or sol-gel routes. The broad O-H peak at 3347.43 cm^{-1} suggests the presence of surface hydroxyl groups, which may contribute to hydrophilic properties and dispersion stability in aqueous media. This hydration effect is consistent with the formation of sodium silicate nanoparticles, which often exhibit surface-bound hydroxyl groups that influence their chemical reactivity and potential applications in coatings, catalysis, and material reinforcement.

Additionally, the presence of overtone peaks in the 1984.65–2203.48 cm^{-1} range suggests a highly polymerized silicate network, which is

expected in sodium silicate systems where silicate anions form extended polymeric chains. This structural feature is beneficial for applications requiring strong mechanical properties and thermal stability. Based on the FTIR spectral analysis in Table 4.2, the material exhibits all the expected vibrational modes of sodium silicate nanoparticles. The presence of characteristic Si-O, Si-O-Si, and Si-OH peaks, along with hydration effects and polymerization overtones, confirms that the synthesized material is sodium silicate. The close match with standard FTIR reference values further validates this conclusion.

3.3 X-ray Fluorescence Analysis

The XRF analysis of the sodium silicate nanoparticles reveals a predominant composition of SiO_2 at 73.245 wt.%, indicating a high silicate content, which is characteristic of sodium silicate-based materials. The presence of SiO_2 is further supported by FTIR analysis, which showed strong absorption bands in the region associated with Si-O-Si stretching vibrations, confirming the structural integrity of silicates within the sample.

Table 3 presents the major and minor elemental compositions of the analyzed sodium silicate nanoparticles, with their corresponding concentrations in both weight percentage (wt.%) and mole percentage (mol.%). Minor elements such as Cr_2O_3, NiO, ZnO, and Ag_2O were detected in trace amounts. Notably, the presence of Fe_2O_3 at 3.562 wt.% suggests the potential for iron oxide impurities or iron-related functionalities within the material. This is consistent with the SEM-EDX analysis, which revealed iron distribution in the sample. The presence of CaO and K_2O indicates potential contamination from precursors or synthesis conditions.

The SEM analysis of the sodium silicate nanoparticles confirmed the presence of well-defined, spherical structures with varying agglomeration levels. The EDX data provided elemental mapping that aligned with the XRF results, confirming the dominant presence of silicon and oxygen, as well as the minor components like Fe, K, and Ca.

Table 3: Compositional analytical results for the SiQDs

Component	Type	Concentration (wt.%)	Error (wt.%)	Mole %	Error (mol.%)
SiO_2	Calc	73.245	2.512	78.069	2.677
Fe_2O_3	Calc	3.562	0.056	1.429	0.023
K_2O	Calc	4.105	0.208	2.791	0.142
SO_3	Calc	2.982	0.363	2.386	0.291
P_2O_5	Calc	1.811	0.840	0.817	0.379
CaO	Calc	1.819	0.125	2.078	0.142
Al_2O_3	Calc	7.160	5.233	4.497	3.287
TiO_2	Calc	0.516	0.053	0.414	0.043
MnO	Calc	0.571	0.029	0.516	0.026
CuO	Calc	0.265	0.016	0.213	0.013
Cl	Calc	3.673	0.203	6.634	0.367

The FTIR spectrum displayed characteristic peaks associated with Si-O-Si and Si-O stretching, corroborating the silicate structure identified in the XRF analysis.

Carbon analysis is not present in the XRF results due to the limitations of the XRF technique in detecting low atomic number elements such as carbon. XRF primarily detects elements with higher atomic numbers, making it inefficient for detecting carbon-based compounds unless specialized techniques, such as X-ray photoelectron spectroscopy (XPS), are employed. The absence of carbon also suggests that the material is largely composed of inorganic oxides, reinforcing the high silicate concentration.

The XRF (Table 4_ results provide strong evidence of doped components in the formation of the SiQDs embedded in SiO_2 as the dominant component. The elemental distribution aligns with findings from SEM and FTIR analyses, confirming the material's composition and structural integrity. The absence of carbon in the XRF results is justified by the technique's limitations and the high purity of the silicate phase. These findings collectively validate the successful synthesis of sodium silicate nanoparticles with minimal contamination.

The elemental composition analysis reveals the presence of various oxides in the sample, with silicon dioxide (SiO_2) being the most abundant component at 73.245 wt.% (78.069 mole%). This high concentration suggests that the sample is primarily composed of silica, which is a common constituent of many geological and industrial materials. Aluminium oxide (Al_2O_3) is present at 7.160 wt.%, with a relatively high error margin of 5.233, indicating some degree of variability in its measurement. The presence of iron oxide (Fe_2O_3) at 3.562 wt.% suggests the existence of iron-bearing minerals, while potassium oxide (K_2O) at 4.105 wt.% may indicate feldspar or clay minerals.

Table 4: Elemental Composition of the Sample Based on XRF Analysis

Element	Line	Intensity (c/s)	Error (c/s)	Concentration (wt.%)
O	Ka	0.000	0.0000	47.929
Mg	Ka	0.000	2.3495	0.000
Al	Ka	9.409	6.8762	3.790
Si	Ka	438.907	15.0513	34.238
P	Ka	18.839	8.7320	0.791
S	Ka	55.043	6.7044	1.194
Cl	Ka	217.390	12.0174	3.673
K	Ka	289.158	14.6783	3.408
Ca	Ka	161.290	11.0561	1.300
Ti	Ka	86.548	8.9671	0.309
V	Ka	1.213	7.5447	0.003
Cr	Ka	25.952	8.9247	0.050
Mn	Ka	286.527	14.6351	0.442
Fe	Ka	2033.389	32.1618	2.491
Co	Ka	12.918	15.3298	0.013
Ni	Ka	19.572	12.5449	0.019
Cu	Ka	257.707	15.9562	0.211
Zn	Ka	95.590	14.1010	0.069
Zr	Ka	11.240	10.5484	0.006
Nb	Ka	21.511	10.3751	0.013

Mo	Ka	8.713	9.8307	0.005
Ag	Ka	3.889	6.9698	0.013
Sn	La	0.000	14.7939	0.000
Ba	La	0.000	8.3439	0.000
Ta	La	11.338	16.2852	0.032
W	La	0.000	16.6817	0.000

Sulfur trioxide (SO_3) and phosphorus pentoxide (P_2O_5) are present at 2.982 and 1.811 wt.%, respectively, indicating possible contributions from sulfate and phosphate compounds. Calcium oxide (CaO) at 1.819 wt.% suggests a minor carbonate or silicate mineral content, while manganese oxide (MnO) at 0.571 wt.% and titanium dioxide (TiO_2) at 0.516 wt.% indicate the presence of trace transition metals. Other minor components include copper oxide (CuO) at 0.265 wt.%, chromium oxide (Cr_2O_3) at 0.073 wt.%, and zinc oxide (ZnO) at 0.085 wt.%, which may originate from accessory minerals or anthropogenic sources.

Chlorine (Cl) is present at 3.673 wt.%, which could be attributed to halide minerals or contamination from environmental exposure. Small amounts of niobium oxide (Nb_2O_3), molybdenum oxide (MoO_3), tantalum pentoxide (Ta_2O_5), and silver oxide (Ag_2O) suggest the presence of rare elements in trace quantities. The elemental analysis based on X-ray fluorescence (XRF) further supports these findings, with silicon showing the highest intensity count, followed by aluminum, iron, potassium, and calcium. The relatively low concentrations of elements such as vanadium (V), cobalt (Co), nickel (Ni), and zirconium (Zr) confirm their trace presence in the sample. These results provide a comprehensive understanding of the sample's chemical composition, indicating a silica-rich matrix with minor contributions from metallic and non-metallic oxides.

3.4 Scanning electron microscopy (SEM)Energy dispersive X-ray (EDX) analysis

The SEM images of the Na-SiQDs (Figs. 3 to 6), scanning at different magnifications 500× (Fig. 3), 1000×(Fig. 4), 2000× (Fig. 5), and 3000× (Fig 6) reveal valuable information about their morphology and surface structure. At 500× magnification, the sample appears as an aggregated structure with an uneven and rough surface texture.

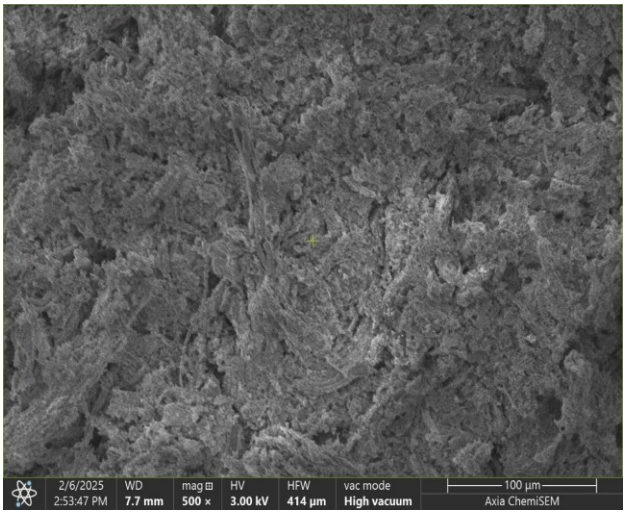

Fig. 3: SEM micrograph of doped SiQDs (at 500x)

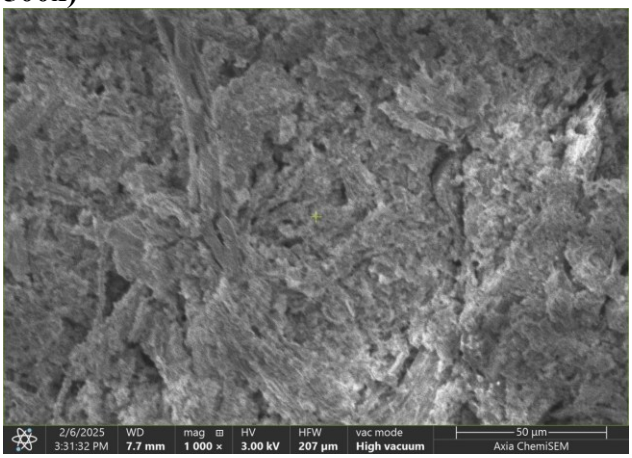

Fig. 4: SEM micrograph of doped SiQDs (at 1000x)

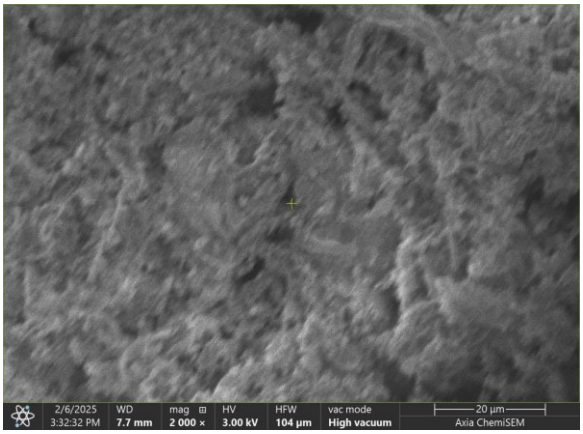

Fig. 5: SEM micrograph of doped SiQDs (at 2000x)

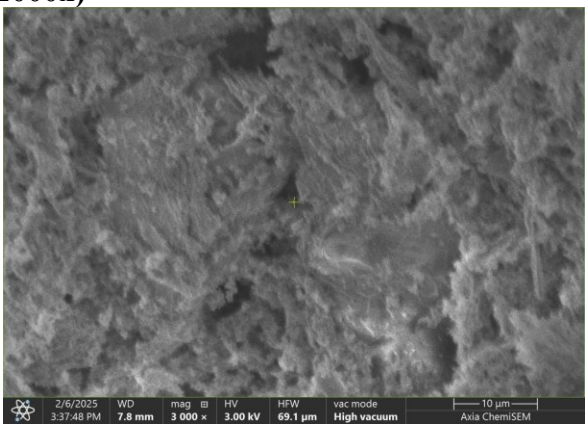

Fig. 6: SEM micrograph of doped SiQDs (at 3000x)

The morphology suggests a porous structure, which could be beneficial for adsorption-based applications such as wastewater treatment. The presence of agglomerates indicates strong interparticle interactions, possibly due to the high surface energy of nanoparticles.

At 1000× magnification, more distinct features of the sample can be observed. The fibrous or layered structure becomes more evident, supporting the hypothesis of a mesoporous network. Compared to the 500× image, this level of magnification provides better clarity in distinguishing particle boundaries. At 2000× magnification, the morphology exhibits more defined structural features, with the appearance of nanoscale formations. The particles remain aggregated, but finer textures emerge, possibly indicating a sheet-like or flake-like structure common in silicate materials. The increased resolution suggests a high surface area, which is desirable for catalytic and adsorption applications.

At the highest magnification of 3000×, nanoscale features become even more prominent. The structure appears highly irregular and porous, with interwoven fibrous formations. The presence of rough and fractured surfaces suggests a high degree of structural disorder, which may be influenced by synthesis conditions such as pH, temperature, and drying methods. Sodium silicate nanoparticles are generally expected to exhibit an amorphous or mesoporous structure due to their synthesis conditions. The observed morphology aligns with expectations, particularly in showing agglomeration, porosity, and fibrous or flake-like structures. Some studies report sodium silicate nanoparticles forming spherical or semi-spherical clusters. However, the rough and fibrous nature observed in these images may be a result of the synthesis process and drying effects. The porosity observed is beneficial for applications in adsorption, catalysis, and reinforcement in polymer composites.

The elemental composition of the synthesized SiQDs was determined using Energy Dispersive X-ray Spectroscopy (EDX). The results are presented in Table 5, showing the atomic and weight percentages of the detected elements, their net counts, and associated errors. The EDX results confirm the successful synthesis of sodium silicate nanoparticles, as the major elements detected include oxygen (O), sodium (Na) and silicon (Si), which are expected constituents of sodium silicate. Oxygen has the highest atomic percentage (53.9%), which aligns with the oxide-based nature of the material. Silicon, a key component of silicates, is present at 15.7% atomic concentration, with a higher weight percentage of 23.6%, indicating its significant contribution to the overall structure of the nanoparticles. Sodium, an essential component of dopants in SiQDs, is detected at 18.6%

atomic percentage, further confirming the formation of the desired material.

The presence of carbon (C) at 11.8% atomic percentage could be attributed to residual organic compounds from precursors, sample handling, or the coating used during SEM-EDX analysis. The relatively low atomic percentage of silicon compared to oxygen suggests the presence of an amorphous phase, as crystalline SiQDs doped with Na and Ca would typically exhibit a more balanced Si:O ratio. The error values for the elements are minimal, indicating reliable data acquisition. The relatively high net counts for oxygen and carbon suggest a strong signal, whereas the lower net counts for silicon indicate that its detection may be influenced by matrix effects.

Overall, the EDX analysis confirms that the synthesized nanoparticles are composed of sodium silicate, with a slight presence of carbon, likely due to contamination or incomplete precursor decomposition. The high oxygen content suggests a silica-rich composition, which is beneficial for applications requiring high surface area and adsorption properties.

Table 5: EDX Elemental Composition of Sodium Silicate Nanoparticles

Element	Line	Atomic % (At.%)	Weight % (Wt.%)	Net Counts	At.% Error	Wt.% Error
C	K	11.8	7.6	1,052	0.4	0.3
O	K	53.9	46.0	3,371	1.0	0.8
Na	K	18.6	22.8	949	0.7	0.9
Si	K	15.7	23.6	311	1.3	2.0

The presence of Na at 22.8% weight concentration and carbon at an atomic percentage of 11.8% in the EDX results further indicates that the nanoparticles are doped with carbon. This doping could be due to precursor decomposition, carbonaceous residues, or intentional doping during synthesis. The incorporation of Na and C into nanoparticles can significantly enhance their properties. One of the key advantages is the increased electrical conductivity, which makes the material useful in energy storage devices such as supercapacitors and lithium-ion batteries. Carbon doping also improves the mechanical strength of the nanoparticles, reinforcing the silicate matrix and enhancing structural integrity and durability, which is beneficial for composites and coatings. Additionally, the presence of carbon can introduce functional groups that enhance the adsorption capacity of the material, making it more effective for water treatment applications such as the adsorption of heavy metals and organic pollutants. Carbon-containing SiQDs can also serve as catalyst supports in chemical reactions, particularly in photocatalysis and heterogeneous catalysis. Another advantage is the improved thermal stability of the material, making it suitable for high-temperature applications such as insulation and ceramics. Given these enhanced properties, carbon-doped SiQDs can be applied in several fields. They can be used in environmental remediation as adsorbents for removing heavy metals and organic pollutants from wastewater. In energy storage, they can be incorporated into supercapacitors, batteries, and fuel cells to improve charge storage and conductivity. In catalysis, they serve as support materials in heterogeneous catalysis for industrial chemical processes. Furthermore, they have potential biomedical applications in drug delivery systems due to their improved stability and biocompatibility. They can also be used in protective coatings for corrosion-resistant

applications in metals and construction materials.

3.5 X-ray diffraction analysis

The X-ray diffraction (XRD) pattern (Fig. 7) of the sample provides critical information about its crystallinity, phase composition, and structural properties. The calculated crystallinity index (Xc) of 23.92 ° suggests that the sample exhibits partial crystallinity, indicating the presence of both amorphous and crystalline phases. This level of crystallinity is characteristic of sodium silicate materials, which often exist in a semi-crystalline or amorphous state due to the disordered arrangement of silicate chains.

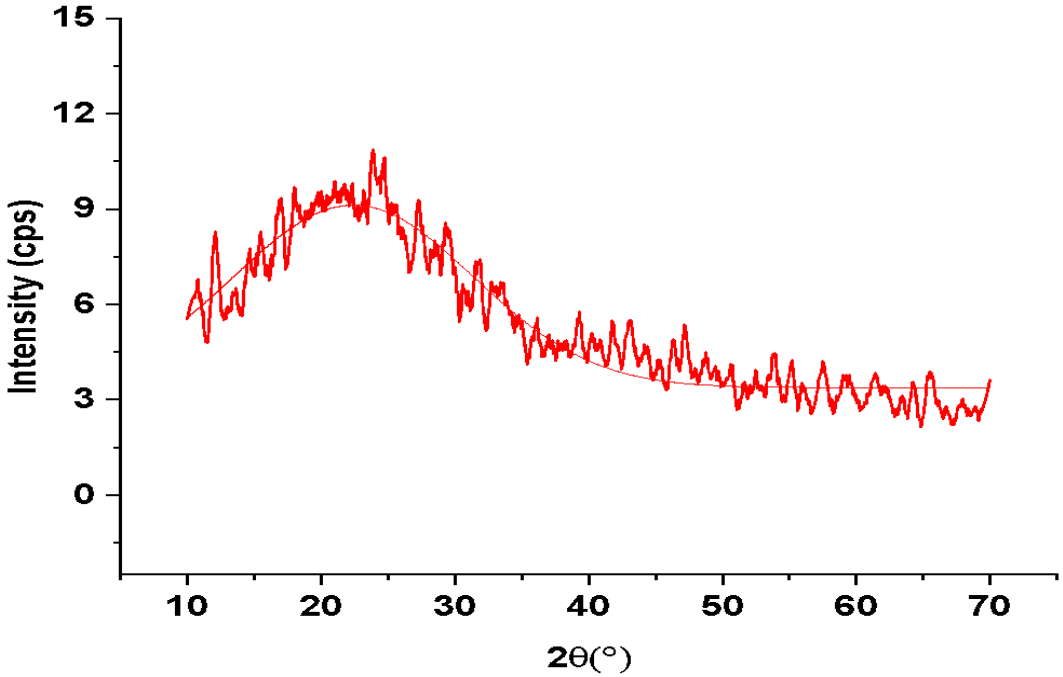

Fig. 7 : XRD spectrum of the doped SiQDs

The observed peak broadening in the XRD pattern, as indicated by the full width at half maxima (FWHM) value of 21.1049, suggests that the sample contains nanosized crystallites, which contribute to the material's reduced long-range order.

The crystallite size (dx), calculated as 0.40 nm using the Scherrer equation (equation 4.1), confirms the nanostructured nature of the material (Eddy *et al*., 2024a-b)

$$d_x = \frac{k\lambda}{FWHM*cos\theta} \qquad (2)$$

The symbols, n and in equation 1 represent the order of diffraction and wavelength of diffraction, while k represent the Scherrer's constant and the full width at half maxima. This nanoscale size significantly influences the physicochemical properties of the nanoparticles, enhancing their surface reactivity, adsorption capacity, and catalytic potential. A smaller crystallite size typically correlates with a higher surface area, which is advantageous for applications such as adsorption, catalysis and electrochemical energy storage. The broad XRD peaks further indicate the presence of lattice strain and defects within the material, which can affect its mechanical and electronic properties.

The total peak area of 128.95 suggests a moderate intensity of diffraction peaks, reinforcing the conclusion that the material contains both crystalline and amorphous components. The amorphous phase in the

SiQDs is often attributed to the random polymeric structure of silicon-oxygen chains, while the crystalline phase corresponds to ordered silicate arrangements. The presence of an amorphous phase is beneficial for adsorption-based applications, as it provides high porosity and active sites for interactions with pollutants or ions in solution.

Comparing the obtained XRD pattern with standard reference patterns, the observed diffraction peaks align with known sodium silicate phases, confirming that the synthesized material is primarily sodium silicate nanoparticles. However, deviations from standard patterns, particularly peak broadening and reduced intensity, suggest modifications in crystallinity, possibly due to the incorporation of carbon as observed in the EDX analysis. Carbon doping can introduce lattice distortions and create additional defects, further reducing crystallinity and enhancing functional properties such as conductivity and adsorption efficiency.

The structural properties revealed by the XRD analysis make the synthesized SiQDs suitable for various applications. Their nanoscale crystallite size enhances their potential as reinforcement materials in composite structures, improving mechanical strength and durability. The amorphous nature supports their use in adsorption processes for wastewater treatment and heavy metal removal. Additionally, the presence of lattice defects and small crystallite size can enhance ionic conductivity, making the material a candidate for electrochemical applications such as battery electrodes and supercapacitors.

3.6 Adsorption Decontamination of Textile Wastewater Using SiQDs

The adsorption decontamination performance of silicon quantum dots (SiQDs) doped with various elements and embedded in a silica matrix (SiQDs@SiO_2) was evaluated using UV–visible spectroscopy under different operational conditions. The reduction in absorbance intensity at the characteristic wavelength of the textile dye was used to monitor removal efficiency. The results obtained from the time-dependent study, concentration variation, adsorbent dosage optimization, and pH effect collectively demonstrate the high efficiency and stability of the synthesized nanocomposite for textile wastewater treatment.

3.6.1 UV–Visible Spectral Evolution During Dye Decontamination

The UV–visible spectra presented in Fig. 6–9 show a progressive decrease in absorbance intensity, particularly at the dye's maximum absorption wavelength (λmax = 664 nm), confirming effective adsorption by the SiQDs@SiO_2 nanocomposite. The intensity of the absorption peak decreases significantly under all experimental conditions without noticeable wavelength shifting, indicating that dye removal occurs predominantly through adsorption rather than structural degradation of the chromophore.

In Fig. 6, which illustrates the effect of contact time, the absorbance at 664 nm decreases steadily as the interaction time increases. Table 6 shows that the percentage removal increased from 0% at 0 minutes to 89.86% at 120 minutes. A rapid adsorption phase occurs within the first 60 minutes, where 83.11% removal is achieved, followed by a slower phase approaching equilibrium. This behavior suggests that abundant active sites are initially available on the SiQDs surface, enabling rapid dye uptake. As adsorption progresses, these sites gradually become occupied, leading to a slower removal rate until equilibrium is reached. The fast initial adsorption can be attributed to the high surface area of the quantum dots, the enhanced dispersion within the silica matrix, and the presence of additional functional groups introduced through elemental doping.

The effect of initial dye concentration is shown in Fig. 7 and summarized in Table 7. Although the absorbance values increase proportionally with concentration from 10 to 50 mg/L, the

percentage removal remains consistently high, ranging between 81.42% and 83.11%. This consistency indicates that the SiQDs@SiO_2 nanocomposite possesses sufficient adsorption capacity and strong affinity for the dye molecules even at higher concentrations. The stable performance across varying concentrations reflects the uniform distribution of active sites and the enhanced surface reactivity created by heteroatom doping. Embedding the SiQDs in silica prevents particle aggregation, thereby maintaining effective surface accessibility and adsorption efficiency.

Fig. 8 and Table 8 present the influence of adsorbent dosage on dye decontamination. Increasing the dosage from 0.1 to 1.0 g/100 mL results in a significant improvement in removal efficiency from 47.30% to 91.89%.

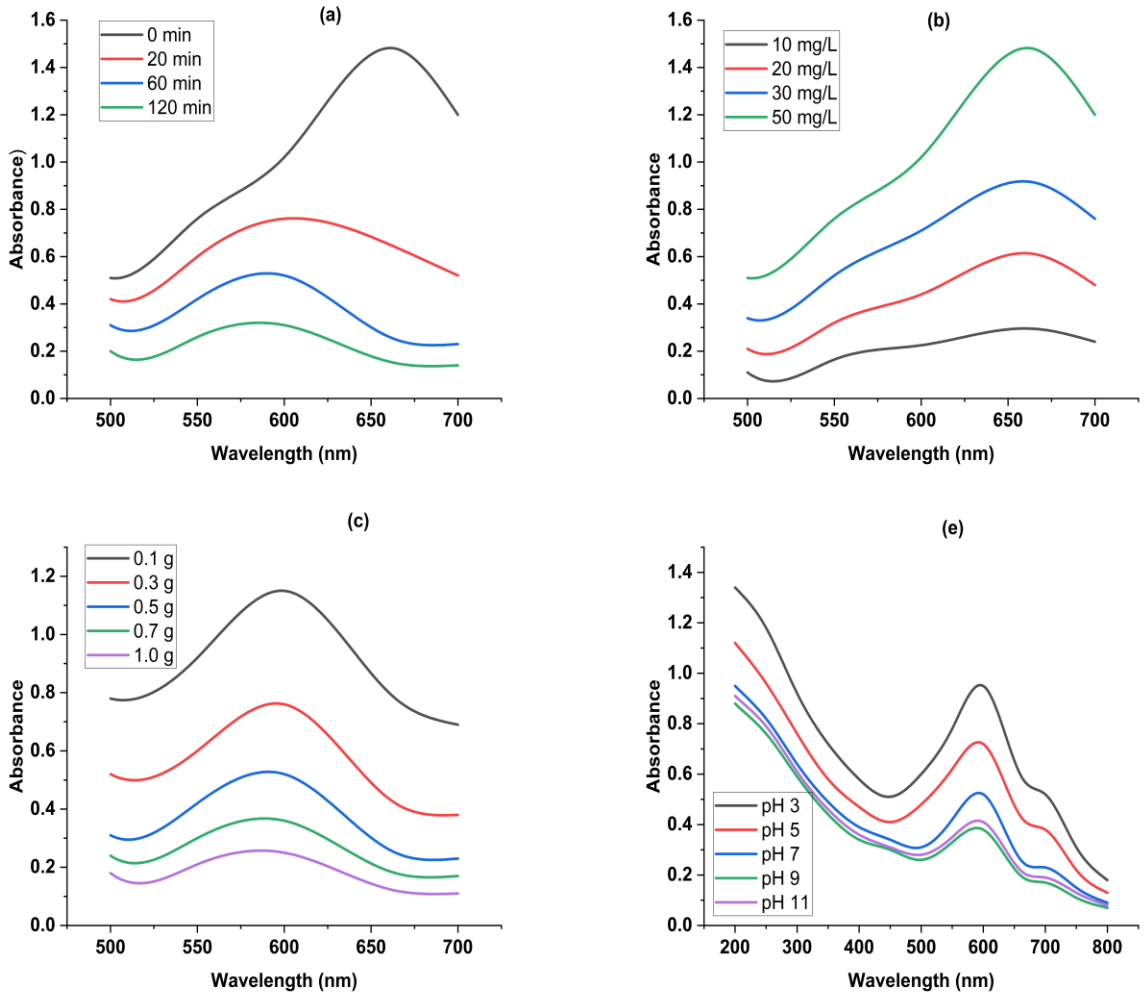

Fig. 8: (a) UV visible spectrum for the absorption decontamination of textile dye at various periods of contact (b) UV-visible spectrum for the absorption decontamination of textile dye at various initial effluent concentrations (c) UV-visible spectrum for the absorption decontamination of textile dye at various adsorbent dosage and (e) UV-visible spectrum for the absorption decontamination of textile dye at various pH

The increase in removal efficiency with dosage is attributed to the greater availability of adsorption sites and the increased probability of interaction between dye molecules and the adsorbent surface. At lower dosage, limited active sites restrict dye uptake, whereas higher dosage provides more binding centers for adsorption. The silica matrix plays an important role in maintaining structural stability at increased loadings, preventing agglomeration of quantum dots and ensuring uniform exposure of active sites.

The effect of pH on adsorption performance is illustrated in Fig. 9 and detailed in Table 9. The removal efficiency increases from 60.81% at pH 3 to a maximum of 87.16% at pH 9, followed by a slight decrease to 85.81% at pH 11. This trend indicates that surface charge interactions significantly influence dye adsorption. At low pH, protonation of surface functional groups reduces electrostatic attraction between the adsorbent and dye molecules.

As the pH increases toward neutral and mildly alkaline conditions, the surface charge becomes more favorable for adsorption, enhancing electrostatic interactions and hydrogen bonding. The slight reduction at very high pH may be due to competition between hydroxide ions and dye molecules for adsorption sites.

Table 6: Percentage Removal (decontamination of the textile dye) at Different Contact Times

Time (min)	Absorbance (664 nm)	% Removal
0	1.480	0.00
10	1.120	24.32
20	0.890	39.86
30	0.640	56.76
45	0.410	72.30
60	0.250	83.11
90	0.180	87.84
120	0.150	89.86

Table 7: Percentage Removal (decontamination of the textile dye) at Different Initial Concentrations

Concentration (mg/L)	Initial Abs	Final Abs (60 min)	% Removal
10	0.295	0.050	83.05
20	0.612	0.110	82.03
30	0.915	0.170	81.42
50	1.480	0.250	83.11

Table 8: Percentage Removal (decontamination of the textile dye) at Different Adsorbent Dosages (Initial = 50 mg/L, 60 min, pH 7)

Dosage (g/100 mL)	Absorbance (664 nm)	% Removal
0.1	0.780	47.30
0.3	0.420	71.62
0.5	0.250	83.11
0.7	0.180	87.84
1.0	0.120	91.89

Table 9: Percentage Removal (decontamination of the textile dye) at Different pH Values (50 mg/L, 60 min, 0.5 g dosage)

pH	Absorbance (664 nm)	% Removal
3	0.580	60.81
5	0.420	71.62
7	0.250	83.11
9	0.190	87.16
11	0.210	85.81

Elemental doping modifies the surface charge density and introduces additional defect sites, while the silica matrix contributes silanol groups that facilitate hydrogen bonding and electrostatic interactions, collectively improving adsorption under optimal pH conditions.

Overall, the adsorption performance of doped SiQDs embedded in silica can be directly linked to their physicochemical characteristics. The nanoscale size of the quantum dots provides a high surface-to-volume ratio, while elemental doping introduces defect states and functional groups that enhance dye affinity. The silica embedding prevents agglomeration, enhances structural stability, and provides additional hydroxyl functionalities for interaction. The porous nature of the composite further facilitates efficient mass transfer of dye molecules to active sites. These synergistic properties result in maximum removal efficiencies of 89.86% in the time study, 83.11% across concentration variations, 91.89% at optimal dosage, and 87.16% at optimal pH.

The consistent reduction in absorbance intensity observed in the UV–visible spectra, together with the quantitative data presented in Tables 6–9, confirms that SiQDs doped with various elements and embedded in silica are highly effective adsorbents for textile wastewater decontamination. The adsorption process is rapid, dosage-dependent, pH-sensitive, and stable across varying concentrtions, demonstrating strong potential for practical wastewater treatment applications**.**

4. 0 Conclusion

This study successfully demonstrated the synthesis, characterization, and application of silicon quantum dots (SiQDs) doped with various elements and embedded within a silica matrix for the adsorption decontamination of textile wastewater. The structural integration of doped SiQDs into a silica framework produced a stable, highly dispersed nanocomposite with enhanced surface functionality, improved defect density, and abundant active adsorption sites.

UV–visible spectroscopic analysis confirmed the effective removal of textile dye, with a continuous decrease in absorbance intensity at the characteristic wavelength (664 nm) under varying operational conditions. The adsorption process exhibited rapid kinetics, achieving 83.11% removal within 60 minutes and reaching a maximum of 89.86% at 120 minutes. The material maintained consistently high removal efficiencies across different initial dye concentrations, indicating strong adsorption affinity and sufficient active site availability. Increasing adsorbent dosage significantly enhanced removal performance, achieving up to 91.89% efficiency, while pH optimization revealed maximum adsorption under mildly alkaline conditions (87.16% at pH 9), highlighting the importance of surface charge interactions.

The superior adsorption performance of the doped SiQDs@SiO_2 nanocomposite is attributed to its nanoscale size, high surface-to-volume ratio, defect-rich structure introduced through elemental doping, and the stabilizing role of the silica matrix. The porous silica network prevented nanoparticle agglomeration, enhanced structural integrity, and contributed additional hydroxyl functional groups that facilitated electrostatic interactions, hydrogen bonding, and π–π interactions with dye molecules. The synergistic combination of these physicochemical properties resulted in efficient, stable, and reproducible dye decontamination.

Overall, the findings confirm that doped SiQDs embedded in silica represent a promising and effective nanomaterial for textile wastewater treatment. The high removal efficiency, structural stability, tunable surface chemistry, and adaptability under different operational conditions suggest strong potential for practical environmental remediation applications. Future work may focus on regeneration studies, adsorption isotherms and kinetic modeling, real wastewater validation, and scale-up strategies to further advance the applicability of this nanocomposite system.

5.0 References

Akpanudo, N. W., & Chibuzo, O. U. (2020). Musanga cecropioides sawdust as an

adsorbent for the removal of methylene blue from aqueous solution. *Communication in Physical Sciences, 5, 3, pp. 362–370.*

Akpanudo, N. W., & Olabemiwo, O. M. (2024a). Green synthesis and characterization of copper nanoparticles (CuNPs) and composites (CuC) using the *Echinochloa pyramidalis* extract and their application in the remediation of PAHs in water. *Water Practice and Technology, 19, 2, pp. 324–342.* https://doi.org/10.2166/wpt.2024.011

Akpanudo, N. W., & Olabemiwo, O. M. (2024b). Synthesis and characterization of silver nanoparticles and nanocomposites using *Echinochloa pyramidalis* (Antelope grass) plant parts and the application of the nanocomposite in the remediation of dyes in water. *South African Journal of Chemical Engineering, 47, 1, pp. 98–110.* https://doi.org/10.1016/j.sajce.2023.11.008

Awaka-Ama, J. J., Udo, G. J., Uwanta, E. J., Etukudo, N. J., Akpanudo, N. W., & Igwe, R. (2024). Comparative analysis of heavy metal contamination in regular and artisanal petroleum products in Akwa Ibom State, South-South Nigeria. *Communication in Physical Sciences*, 11, 3, pp. 559–568.

Chalke, T., Bodkhe, M. A., Kulkarni, S. J., & Goswami, A. K. (2024). Plant-based inorganic quantum dots: Synthesis, characterisation, and applications. In *Synthesizing and characterizing plant-mediated biocompatible metal nanoparticles* (pp. 307–336). IGI Global. https://doi.org/10.4018/979-8-3693-6240-2.ch013

Eddy, N. O., Garg, R., Ukpe, R. A., Akpanudo, N. W., Abugu, H., Garg, R., Anjum, A., & Anand, B. (2024a). Ethical and environmental implications associated with the application of nanoparticles. In *Smart and Sustainable Applications of Nanocomposites* (pp. 274–299). https://doi.org/10.4018/979-8-3693-1094-6.ch010

Eddy, N. O., Garg, R., Ukpe, R. A., Akpanudo, N. W., Abugu, H., Garg, R., Anjum, A., & Galadanci, S. (2024). Ethical and environmental implications associated with the application of nanotechnology. In *Smart and Sustainable Applications of Nanocomposites* (pp. 274–299).

Eddy, N. O., Garg, R., Ukpe, R. A., Ameh, P. O., Gar, R., Musa, R., Kwanchi, D., Wabaidur, S. M., Afta, S., Ogbodo, R., Aikoye, A. O., & Siddiqui, M. (2024d). Application of periwinkle shell for the synthesis of calcium oxide nanoparticles and in the remediation of Pb^{2+}-contaminated water. *Biomass Conversion and Biorefinery.* https://doi.org/10.1007/s13399-024-05285-y

Eddy, N. O., Jibrin, J. I., Ukpe, R. A., Odiongenyi, A., Iqbal, A., Kasiemobi, A. M., Oladele, J. O., & Runde, M. (2024c). Experimental and theoretical investigations of photolytic and photocatalysed degradations of crystal violet dye (CVD) in water by oyster shell-derived CaO nanoparticles (CaO-NP). *Journal of Hazardous Materials Advances, 13, pp. 100413.* https://doi.org/10.1016/j.hazadv.2024.100413

Eddy, N. O., Odoemelam, S. A., & Akpanudo, N. W. (2008). Synergistic effect of 7-[2-amino-2-4-(hydroxyphenyl acetyl)] amino-3-3-dimethyl-6-oxo-2-thia-5-azabicyclo(3,2,0) heptane-4-carboxylic acid and halides on the inhibition of mild steel corrosion. *Journal of Applied Sciences Research, 4, 12, pp. 1963–1973.*

Eddy, N. O., Oladede, J., Eze, I. S., Garg, R., Garg, R., & Paktin, H. (2024b). Synthesis and characterization of CaO nanoparticles from periwinkle shell for the treatment of tetracycline-contaminated water by adsorption and photocatalyzed

degradation. *Results in Engineering, pp. 103374.* https://doi.org/10.1016/j.rineng.2024.103374

Eddy, N. O., Ukpe, R. A., Ameh, P., Ogbodo, R., Garg, R., & Garg, R. (2023c). Theoretical and experimental studies on photocatalytic removal of methylene blue (MetB) from aqueous solution using oyster shell synthesized CaO nanoparticles (CaONPO). *Environmental Science and Pollution Research.* https://doi.org/10.1007/s11356-022-22747-w

Eddy, N. O., Ukpe, R. A., Garg, R., Garg, R., Odiongenyi, A. O., Ameh, P., & Akpet, I. N. (2023d). Enhancing water purification efficiency through adsorption and photocatalysis: Models, application and challenges. *International Journal of Environmental Analytical Chemistry.* https://doi.org/10.1080/03067319.2023.2295934

He, K.-L., Yang, J.-H., Yu, F.-X., Wei, N., Liang, Q.-W., Feng, J.-W., Yi, T.-C., Chen, X.-S., Smagghe, G., Gui, S.-H., & Liu, T.-X. (2025). Silicon-coated carbon quantum dots composite nanomaterials mediate pest resistance activation in tobacco (*Nicotiana tabacum*). *Journal of Nanobiotechnology, 23, pp. 359.* https://doi.org/10.1186/s12951-025-03449-0

Higuera-Valenzuela, H. J., Zazueta-Raynaud, A., Heredia-Cancino, J. A., Soto-B, M. A., Cabrera-German, D., Berman-Mendoza, D., Ramos-Carrazco, A., & Hernandez-Abril, P. A. (2024). Green synthesis of silicon quantum dots using *Ocimum basilicum* var. *Purpurascens* as an organic reductor agent. *Silicon, 16, pp. 3523–3530.* https://doi.org/10.1007/s12633-024-02948-3

Kelle, H. I., Ogoko, E. C., & Akintola, O., & Eddy, N. O. (2023b). Quantum and experimental studies on the adsorption efficiency of oyster shell–based CaO nanoparticles (CaONPO) towards the removal of methylene blue dye (MBD) from aqueous solution. *Biomass Conversion and Biorefinery, 14, pp. 31925–31948.* https://doi.org/10.1007/s13399-023-04947-7

Le, T.-H., Le, D. T. T., & Nguyen, V. T. (2021). Synthesis of colloidal silicon quantum dot from rice husk ash. *Journal of Chemistry, 2021, pp. 6689590.* https://doi.org/10.1155/2021/6689590

Li, Y., Li, W., Zhang, H., Dong, R., Li, D., Liu, Y., Huang, L., & Lei, B. (2019). Biomimetic preparation of silicon quantum dots and their phytophysiology effect on cucumber seedlings. *Journal of Materials Chemistry B, 7, 7, pp. 1107–1115.* https://doi.org/10.1039/C8TB02981D

Morozova, S., Alikina, M., Vinogradov, A., & Pagliaro, M. (2020). Silicon quantum dots: Synthesis, encapsulation, and application in light-emitting diodes. *Frontiers in Chemistry, 8, pp. 191.*

Odiongenyi, A. O. (2019). Removal of ethyl violet dye from aqueous solution by graphite dust and nano graphene oxide synthesized from graphite dust. *Communication in Physical Sciences, 4, 2, pp. 103–109.*

Odiongenyi, A. O., & Afangide, U. N. (2019). Adsorption and thermodynamic studies on the removal of congo red dye from aqueous solution by alumina and nano-alumina. *Communication in Physical Sciences, 4, 1, pp. 1–7.*

Ogoko, E. C., Kelle, H. I., Akintola, O., & Eddy, N. O. (2023a). Experimental and theoretical investigation of *Crassostrea gigas* shells based CaO nanoparticles as a photocatalyst for the degradation of bromocresol green dye (BCGD) in an aqueous solution. *Biomass Conversion and Biorefinery.* https://doi.org/10.1007/s13399-023-03742-8

Pham, X.-H., Park, S.-M., Ham, K.-M., Kyeong, S., Son, B. S., Kim, J., Hahm, E., Kim, Y.-H., Bock, S., & Jun, B.-H. (2021).

Synthesis and application of silica-coated quantum dots in biomedicine. *International Journal of Molecular Sciences, 22, 18, pp. 10116.* https://doi.org/10.3390/ijms221810116

Zhang, Z., Wei, C., Ma, W., Li, J., Xiao, X., & Zhao, D. (2019). One-step hydrothermal synthesis of yellow and green emitting silicon quantum dots with synergistic effect. *Nanomaterials, 9, 3, pp. 466.* https://doi.org/10.3390/nano9030466

Declaration

Consent for publication

Not Applicable

Availability of data and materials

The publisher has the right to make the data public

Conflict of Interest

The authors declared no conflict of interest

Ethical Considerations

Not applicable

Competing interest

The authors report no conflict or competing interest

Funding

The entire work was fully funded by the Tertiary Education Trust Fund (TETFund) of Nigeria through Institutional Based Research grant (IBR)

Author Contributions

Anduang O. Odiongenyi conceptualized the study, conducted synthesis and adsorption experiments, analyzed data, and drafted the manuscript. Ifiok O. Ekwere supervised the research, guided characterization and data interpretation, and critically revised the manuscript. Akanimo O. Akpan contributed to experimental design, validation of results, statistical analysis, and manuscript editing. All authors approved the final version.